SUPPLEMENT:

Multi-decadal basal slip enhancement at Saskatchewan Glacier, Canadian Rocky Mountains

Nathan T. STEVENS[1],Collin J. ROLAND[1], Lucas K. ZOET[1], Richard B. ALLEY[2,3], Dougal D. HANSEN[1], Emily SCHWANS[2]

[1] *Department of Geoscience, University of Wisconsin - Madison, Madison, WI, USA*

[2] *Department of Geosciences, Pennsylvania State University, University Park, PA, USA*

[3] *Earth and Environmental Systems Institute, Pennsylvania State University, University Park, PA, USA*

Correspondence: Nathan T. Stevens <ntstevens@wisc.edu>

OVERVIEW

This supplement provides a summary of ice-surface DEM and velocity observations used in this study and a additional details on our seismic analyses to derive ice-thicknesses, inversions for internal deformation velocities, and propagation of uncertainties.

ICE-SURFACE DEMS AND VELOCITIES

We extracted velocity estimates and uncertainties in the upper and lower sectors from Meier (1957); Mattar and others (1998); Van Wychen and others (2018), which are summarized in Table S1. Uncertainties in from Meier (1957) were included in their text for annual values and estimated from their Table 13 for melt-season values. We used generalized uncertainties for InSAR measurements presented in the text of Mattar and others (1998), but uncertainties for laser rangefinder estimates were not presented in their study. As such, we assumed them to be of a similar scale to theodolite and post-processed GNSS measurements, so we assumed a value between those published in Meier (1957) and our results in 2019. Van Wychen and others (2018) reported uncertainties on RADARSAT-2 based velocities of 5-10 m for their 2011 measurement, so we chose to use the higher value in our analyses. Ice-surface DEMs in this study were largely sourced from Tennant and Menounos (2013) and we provide a summary of their Tables 2 and 3 in Table S2. We provided matching information on the GMTED10 DEM (Danielson and Gesch, 2011) used to supplement exposed rock elevation estimates and documented our measurements in a similar manner.

GNSS VELOCITY PROCESSING

Continuous Data Processing

We display post-processed data from ROV1 at successive stages of cleaning as described in the main text in Figure S1. We also display the windowed-average positions (Fig. S1d) and velocity uncertainties (Fig. S1e) estimated during the rolling-window WLS estimation of surface velocities at ROV1 (Fig 3c, main text). We inspect data-model residuals for displacements in Fig. S1f and find that they are of a similar scale as data uncertainties (e.g., Table S2). In conjunction with small velocity uncertainties, these small misfits support the use of a 4-hour window for estimating surface velocities in the main text.

Campaign Velocity Field

A map of the velocity field from campaign GPS measurements is shown in Figure S2. We found similar velocity values as the long-term campaign GPS surveys, but the uncertainties are larger than the estimate at ROV1 (bubbles in Fig. S2a and entry in Table S1). Campaign velocities progressively declined down-glacier to less than 5 m a^{-1}within 200 m of the 2019 terminus. Similarly velocities declined away from the centerline with a minimum value of 27 m a^{-1}near the southeastern glacier margin and 35 m a^{-1}near the former lateral moraine between Saskatchewan Glacier and TG1 (see Fig. 1 in main text) on the northwestern side of the lower sector. These estimate provided a maximum estimate of the marginal slip rates at these two points. Campaign velocities were enhanced in proximity of the overdeepening and down-flow from the bedrock reigel, consistent with expected hydrodynamics near these features (see main text and discussions in Dow and others, 2011, 2014; Patton and others, 2016).

SEISMIC ANALYSES

We collected seismic data at geophone sites in the upper sector were acquired using six DiGOS/OmniRecs DataCube[3] data-loggers with 4.5 Hz HG-6R three-component (3C) geophones installed on the ablation surface in the upper sector between August 14^{th} and 18^{th} 2017. These units acquired data at 400 Hz using a linear-phase finite impulse response (FIR) filter and a gain of 16 dB to digitizing ground acceleration

Year(s)	Upper Sector (6-6)		Lower Sector (14-5/ROV1)		Source	
	Dates	V_{surf} (m a^{-1})	Dates	V_{surf} (m a^{-1})	Data Source	Reference
1952–1953	08/25/52–08/30/53	65.2±0.2			Theodolite	M57
1953	07/25/53–08/30/53	71.1±1.0	07/09/53–09/29/53	37.2±1.0	Theodolite	M57
1953–1954	07/25/53–08/04/54	65.2±0.2	07/09/53–07/23/54	40.2±0.2	Theodolite	M57
1995			Aug 1995–Sep 1995	46.66±0.01	Laser Rangefinder	M98
			Sep 1995–Dec 1995	43.83±0.01	Laser Rangefinder	M98
	11/21/95–11/22/95	78.5±3.3	11/21/96–11/22/95	39.1±3.3	ERS-1/-2 InSAR	M98
1995–1996			Dec 1995–Feb 1995	39.45±0.01	Laser Rangefinder	M98
1996	04/25/96–04/26/96	83.0±1.5	04/25/96–04/26/96	44.7±1.5	ERS-1/-2 InSAR	M98
2011	03/05/11–03/29/11	72±10	03/05/11–03/29/11	42±10	RADARSAT-2 Speckle-Tracking	V18
2019			08/06/19–08/19/19	63.4±0.001	GNSS Antenna Pair	This Study

Table S1. Ice-surface velocities in the upper and lower sectors of Saskatchewan Glacier (Figs. 1b-c), observation dates, and uncertainties. Citation abbreviations: M57 = Meier (1957), M98 = Mattar and others (1998), and V18 = Van Wychen and others (2018).

Ablation Surface Year	Acquisition Date	Vertical Uncertainty (m)	Data Source	Reference
1948	09/19/48	1	Orthophoto	T12/TM13
1955	08/06/55	2	Orthophoto	T12/TM13
1966	08/22/66	1	Orthophoto	T12/TM13
1970	08/18/70	2	Orthophoto	T12/TM13
1974	09/01/74	1	Orthophoto	T12/TM13
1979	07/09/79	1	Orthophoto	T12/TM13
1986*	07/08/86	2	Orthophoto	T12/TM13
1993	09/09/93	1	Orthophoto	T12/TM13
1999	Feb 2000	6	SRTM	T12/TM13
2009	09/30/09	6	SPOT5	T12/TM13
2010	2009–2010	26–30	GMTED10	DG11
2017	08/14/17–08/18/17	1.2	DataCube GPS	This Study
2019	08/01/19–08/19/19	0.005	Emlid GNSS Pair	This Study

Table S2. Ice-surface digital elevation models of Saskatchewan Glacier, observation dates, uncertainties, and source data type. Based on Tabs. 2 and 3 in (Tennant and Menounos, 2013) and results of this study. Citation abbreviations: T12 = (Tennant, 2012), TM13 = (Tennant and Menounos, 2013), DG11 = (Danielson and Gesch, 2011).

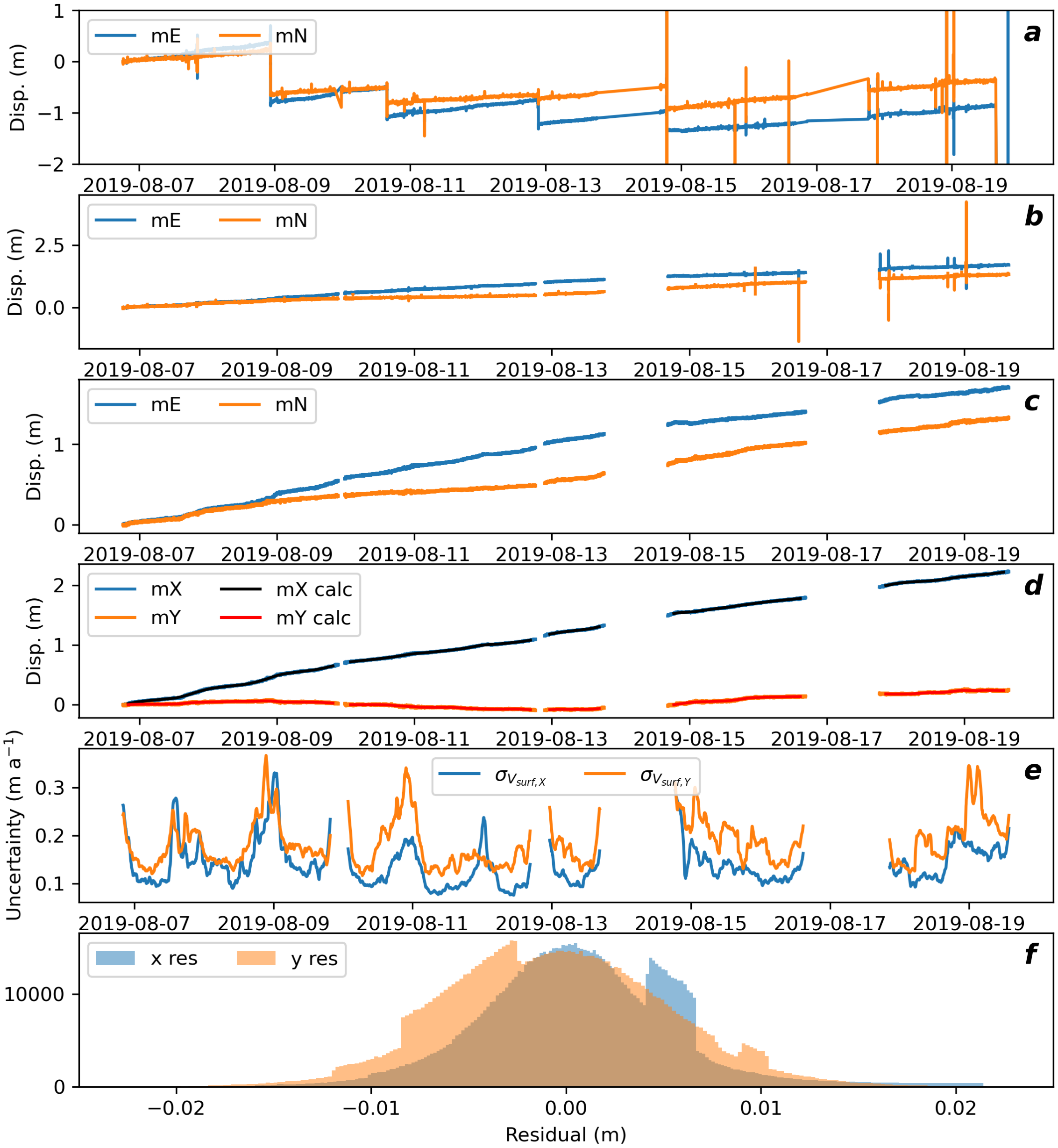

Fig. S1. Continuous GPS displacement processing steps. (a) Post-processed displacements to the north (mN) and east (mE), (b) "stitched" displacements (re-installation displacements modeled out) (c) despiked displacements after two iterations of filtering (d) rotated data into along-flow (mX) and across-flow (mY) bases with average position estimates (calc) from the rolling-window WLS curve fitting, (e) velocity uncertainties from the rolling-window WLS estimates (Fig. 3c in main text), and (f) residuals displacements (e.g., mX – mX calc = x res).

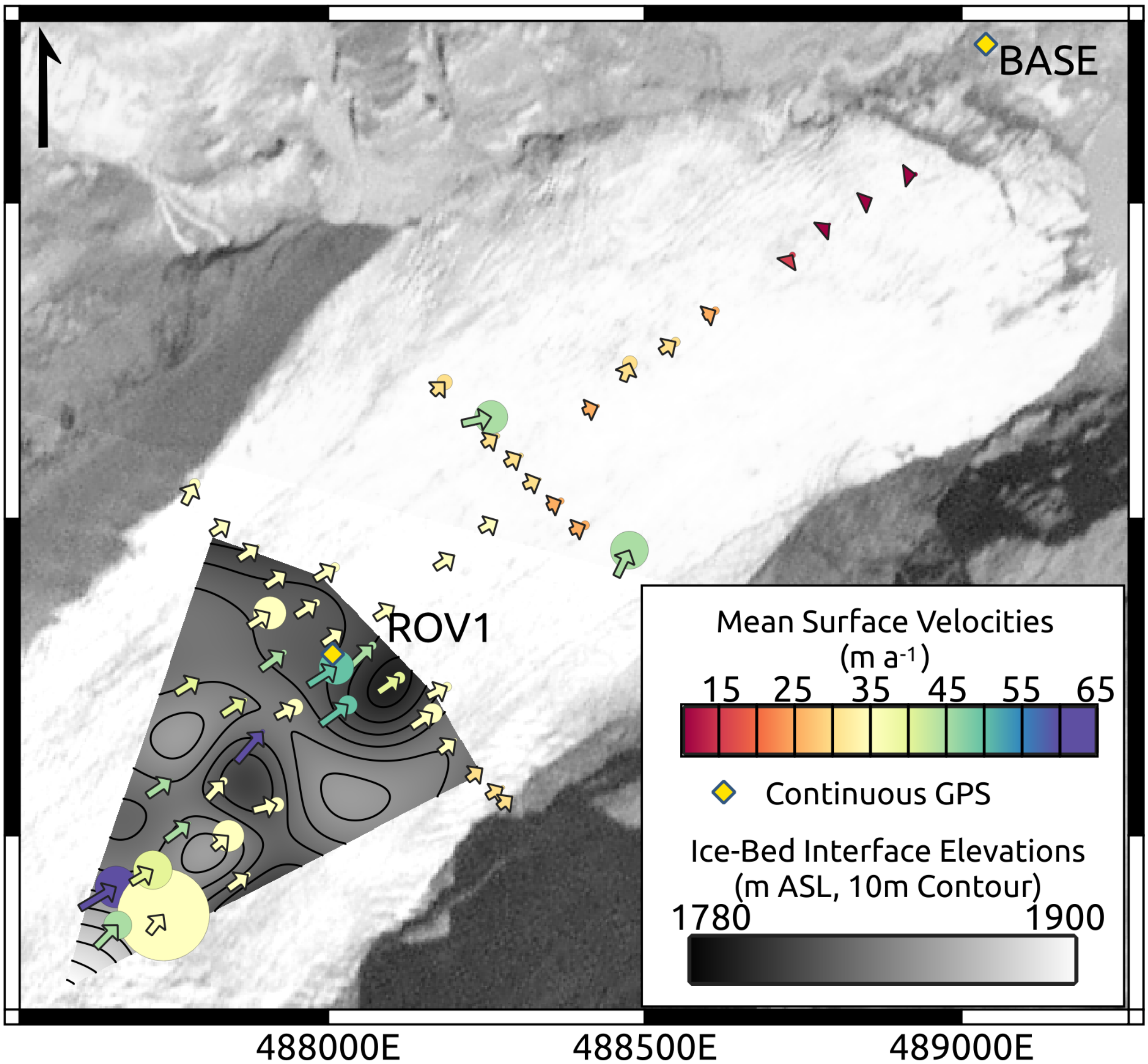

Fig. S2. Campaign GPS velocity field overlain on ice-bed interface topography (Fig. 5a in main text). Arrows are colored and scaled by the mean velocities calculated at each site with observations acquired in between August 1st and 19th. Velocity uncertainties are shown as circles on the ends of velocity arrows and are scaled identically as the arrows.

signals (stations 1–6 in Fig. S3). We used same units as receivers in the active-seismic line acquired in the lower sector on August 18th 2019. Seismic data at geophone sites in the lower sector were acquired between August 1st and 19th 2019 using 12 DTCC SmartSolo IGU-16R 3C geophones (stations 28–40 in Fig S3) and 20 Magseis/Fairfield Zland GEN2 3C geophones (stations 7–27 in Fig. S4) sampling at 1000 Hz using a linear-phase FIR filter and set to a gain of 16 dB. We installed these units in 40 cm deep boreholes finished with a custom-made thermal drill to accommodate their spikes, orient instruments, and enhanced instrument coupling in addition to back-filling borehole anuli with auger cuttings. Geophones in the lower sector were re-installed every 2-5 days to prevent melt-out and three sites were temporary deployments lasting one deployment cycle (stations 22, 23, and 35)

HV Analysis

We estimated horizontal to vertical spectral ratios (HV) from three-hour 3C seismic recordings acquired in evenings shortly after station (re)installation when glaciohydraulic noise sources were diminished, geophone coupling was high quality, and instrument orientations were well constrained (e.g., Carmichael and others, 2012; Stevens and James, 2022). We low-pass filtered and down-sampled data to 100 Hz and segmented them into 120 second long widows with 30 second overlaps. We then calculated HV curves with *OpenHVSR* using the total-energy formulation (Bignardi and others, 2018) for windows that did not contain impulsive signals:

$$HV(f, t \in [t_i, t_j]) = \frac{\sqrt{PSD[u_N(t)]^2 + PSD[u_E(t)]^2}}{PSD[u_Z(t)} \tag{1}$$

with $PSD[u_x(t)]$ the power spectral density of seismometer component X – N (north), E (east), and Z (vertical) – for time window t. After calculating PSD's but before using Eqn. S1 a Konno-Ohmachi smoothing factor of 60 was applied to each PSD. We then calculated individual HV curves (black lines in Fig. S3), resulting 100's of individual HV curves for each seismic site. Some curves were only calculated between 2–6 Hz to mask highly variable low-frequency HV values. We estimated a representative curve and uncertainties (median and 5th / 95th quantiles, white lines in Fig. S3) at each frequency and manually picked peak HV frequencies to estiamte f_0 on this curve (red vertical line in Fig. S3). To quantify uncertainties on f_0 we automatically picked maximum HV values on individual curves within 1 Hz of the manual f_0 pick and calculated the population mean and standard deviations (blue vertical lines in Fig. S3).

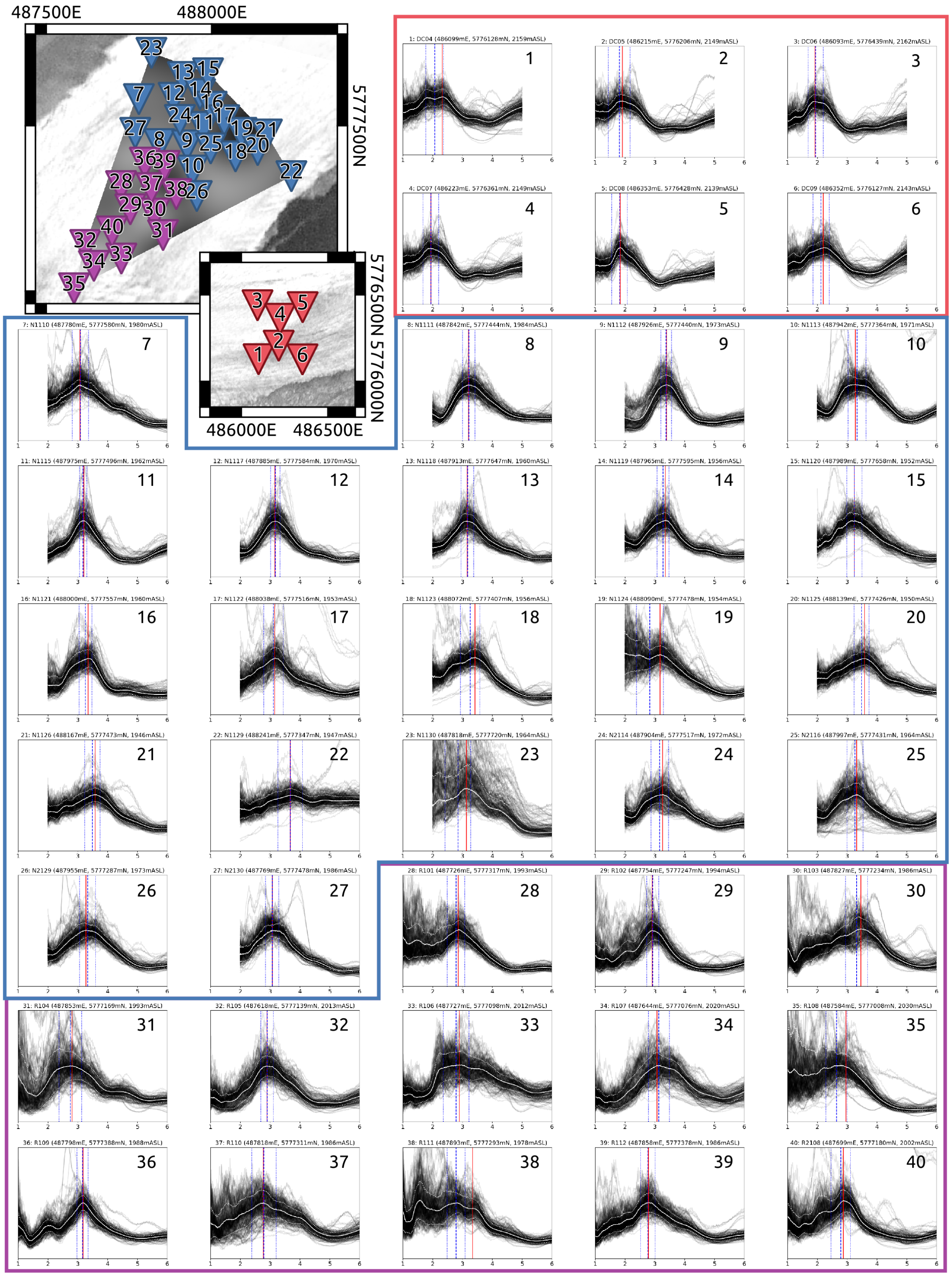

Fig. S3. HV results with reference maps. Stations 1–6 were in the upper sector during 2017 (Fig. 1b in main text) and stations 7–40 were in the lower sector during 2019 (Figs. 1c and 5a in main text). Individual HV curves are shown in black and the median curve and the $5^{th}/95^{th}$ quantiles are shown in white (solid and dashed lines, respectively). Manual picks of f_0 are shown as red vertical lines and the automatically picked f_0 mean and standard deviations are shown as vertical blue lines (dashed and dotted, respectively). HV curves are vertically scaled to the median HV value at the manual f_0 pick and displayed between 1 and 6 Hz. The ice-bed interface elevation map from Fig. 5a (main text) is shown and basemap images are the same as Fig. 1 (main text).

Active Seismic Experiment

To estimate ice seismic velocities conducted an active-source seismic experiment on August 18th 2019. Using a sledgehammer and steel plate, we conducted 18–23 shots at sites spaced 10 meters apart along the glacier's centerline, shooting into the 32 active geophone sites geophones and seven additional DataCubes placed in a linear array (see Figure S4). An eighth DataCube used as the shot timer that was moved to each shot location (zero-offset trace in Fig. S4b). We manually analyzed median-stacked common shot-point (CSP) gathers from 13 shot-points, picking direct P-wave and ground-roll (Rayleigh-wave) arrival times for all geophones and receivers (example in Fig. S4b). Next, we calculated phase velocities and uncertainties with a WLS linear fitting to travel-time versus offset (TTvO) data using typical phase-arrival uncertainties of 0.005 sec for P-waves and 0.002 sec for Rayleigh-waves. Finally, we estimated V_S from V_P and V_R values using expected values of V_P/V_S (1.95, e.g., Smith and others, 2015) for glacier ice and V_R/V_S (0.93, e.g., Aki and Richards, 2002) for most earth materials near a free surface.

Ice thickness estimation

Values of f_0 ranged from 2.6–3.7 Hz in the lower sector and from 2.4–3.1 Hz in the upper sector with uncertainties rarely exceeding 0.25 Hz (see bounds in Fig. S3). Composite travel-time vs offset data from 13 CSP gathers resulted in an estimates of $V_P = 3451 \pm 62$ m s^{-1}and $V_R = 1688 \pm 3$ m s^{-1}(Fig. S4c), which converge on an estimate of $V_S = 1740 \pm 168$ m s^{-1}. We used this estimate and f_0 values from HV analyses to calculate ice-thicknesses using Eqn. 6 (main text). Ice-thickness estimates ranged from 122–169 m in the lower sector with uncertainties of 14–29 m and ranged from 211–247 m in the upper sector with uncertainties of 34–56 m. Mean ice-thicknesses were used with GPS/GNSS ice-surface elevation data to calculate ice-bed interface elevations presented in the main text (Fig. 5a).

INVERSIONS AND ERROR PROPAGATION

We used a combination of weighted least squares (numpy.polyfit), nonlinear least-squares (scipy.optimize.curve_fit), and Monte Carlo Markov Chain (MCMC) simulations to estimate model parameters and uncertainties from our observations throughout this study. Where applicable, we used analytic error propagation formulae for simple equations.

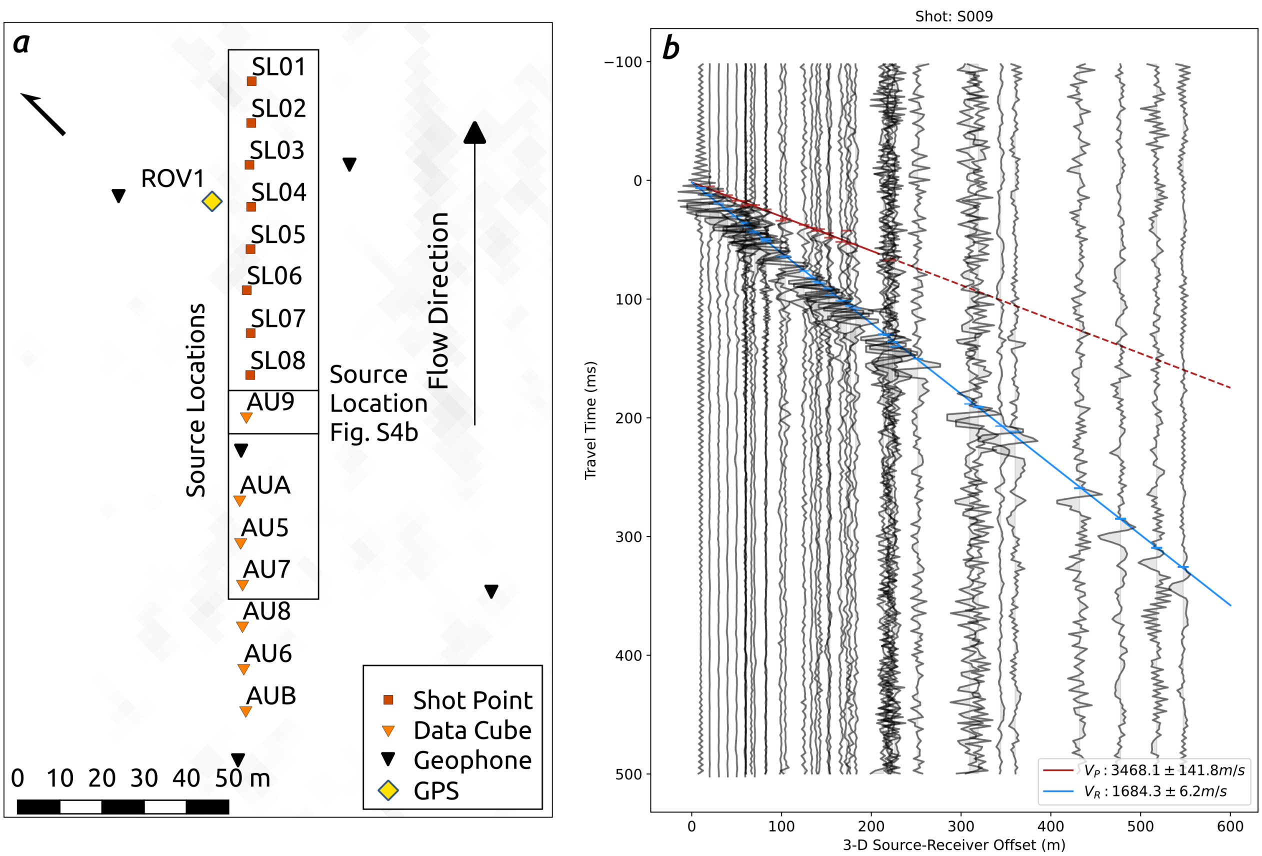

Fig. S4. (a) Overview of the active seismic experiment shooting geometry and positions of supplementary geophones (orange triangles) with the location of an example CSP gather shown. (b) Example TTvO analysis on a 19-fold, median stacked CSP gather at station AU9 with P-wave (red) and Rayleigh wave (blue) picks and move-out curves marked. Velocity estimates for this CSP stack are noted in the lower right corner.

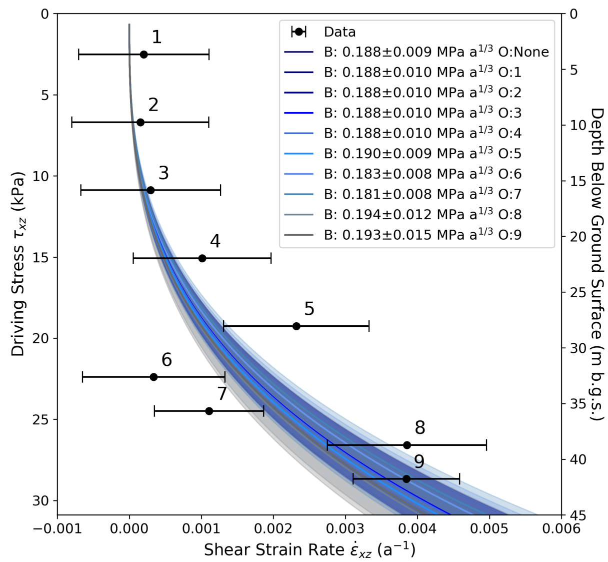

Fig. S5. Borehole deformation data from Meier (1957)(black, lateral errorbars) and effective viscosity inversion results (blue/grey lines and envelopes) from available data and LOOCV analysis. Data omissions (O:) and resultant values of B are given in the legend. Data points are labeled.

Internal Deformation

We show weighted least squares (WLS) inversion results for effective viscosity from borehole deformation data reported by Meier (1957) are shown in Figure S5. Due to the sparse data, we assessed the sensitivity of effective viscosity to individual data-points, conducting a leave-one-out-cross-validation test (LOOCV), the results of which are shown in Fig. S5. Omission of deeper data points tended to increase the drift of estimates, but overall estimates of B remained within 6% of one another. Therefore, we used the average and standard deviation of the ensemble of estimates in our internal deformation calculations.

Inspection of Eqns. 3–5 shows that internal deformation velocities can be estimated as a function of ice-surface elevations, valley profile elevations, ice surface slope, and effective viscosity of the ice. We assumed normally distributed errors for input data and used inverse variances for weights for polynomial fits to ice-surface elevations. Due to the large differences in uncertainties for exposed bedrock elevations and HV-derived bed elevations we applied uniform weighting to polynomial models of the valley shape maintain the importance of bed elevation estimates. We generated perturbed realizations of polynomial fit models using a Latin Hypercube Sampling routine (LHS), incorporating the polynomial models' covariance matrices when drawing samples. Under the assumption that ice-surface slopes and effective viscosity uncertainties did not co-vary with other parameters, we drew samples for each of these parameters from appropriately scaled normal distributions. We then quantified A, P, and H_i from perturbed surfaces, propagated these values through Eqns. 3–5, and inspected the posterior distributions of outputs from each equation. We found that posteriors largely retained the shape of normal distributions. MCMC estimates occasionally produced physically unrealistic values (e.g., S_f=5) that strongly biased calculation of sample means and standard deviations from posterior distributions. As such, we removed outliers that fell outside the 0.1^{st} and 99.9^{th} quantiles of each posterior distribution before calculating representative statistics for parameter estimates in Fig. 6, Table 1, and internal deformation rates presented in Figure 7 in the main text.

DATA AND MATERIALS

Seismic data from Magseis/Fairfield nodal seismometers are archived with the IRIS Data Management Center (IRIS DMC) under network code 1B for 2019. Data collected on SmartSolo instruments are available upon request. All down-sampled seismic data used for HV analyses are included in the data repository linked in the main text.

REFERENCES

Aki K and Richards P (2002) *Quantitative Seismology.* University Science Books, Mill Valley, CA, 2. edition

Bignardi S, Yezzi AJ, Fiussello S and Comelli A (2018) OpenHVSR - Processing toolkit : Enhanced HVSR processing of distributed microtremor measurements and spatial variation of their informative content. *Comput. Geosci.*, **120**(July), 10–20, ISSN 0098-3004 (doi: 10.1016/j.cageo.2018.07.006)

Carmichael JD, Pettit EC, Hoffman M, Fountain A and Hallet B (2012) Seismic multiplet response triggered by melt at Blood Falls, Taylor Glacier, Antarctica. *J. Geophys. Res. Earth Surf.*, **117**(3), 1–16, ISSN 21699011 (doi: 10.1029/2011JF002221)

Danielson J and Gesch D (2011) Global Multi-resolution Terrain Elevation Data 2010 (GMTED2010). *U.S. Geol. Surv. Open-File Rep. 2011-1073*, **2010**, 26

Dow CF, Kavanaugh JL, Sanders JW, Cuffey KM and Macgregor KR (2011) Subsurface hydrology of an overdeepened cirque glacier. *J. Glaciol.*, **57**(206), 1067–1078, ISSN 00221430 (doi: 10.3189/002214311798843412)

Dow CF, Kavanaugh JL, Sanders JW and Cuffey KM (2014) A test of common assumptions used to infer subglacial water flow through overdeepenings. *J. Glaciol.*, **60**(222), 725–734, ISSN 00221430 (doi: 10.3189/2014JoG14J027)

Mattar KE, Vachon PW, Geudtner D, Gray AL, Cumming IG and Brugman M (1998) Validation of alpine glacier velocity measurements using ERS Tandem-Mission SAR data. *IEEE Trans. Geosci. Remote Sens.*, **36**(3), 974–984, ISSN 01962892 (doi: 10.1109/36.673688)

Meier MF (1957) *Mode of Flow of Saskatchewan Glacier, Alberta, Canada*. Ph.D. thesis, California Institute of Technology

Patton H, Swift DA, Clark CD, Livingstone SJ and Cook SJ (2016) Distribution and characteristics of overdeepenings beneath the Greenland and Antarctic ice sheets: Implications for overdeepening origin and evolution. *Quat. Sci. Rev.*, **148**, 128–145, ISSN 02773791 (doi: 10.1016/j.quascirev.2016.07.012)

Smith EC, Smith AM, White RS, Brisbourne AM and Pritchard HD (2015) Mapping the ice-bed interface characteristics of Rutford Ice Stream, West Antarctica, using microseismicity. *J. Geophys. Res. F Earth Surf.*, **120**(9), 1881–1894, ISSN 21699011 (doi: 10.1002/2015JF003587)

Stevens NT and James SR (2022) Capturing the Changing Cryosphere with Seismic Horizontal-Vertical Spectral Ratios. *FastTIMES*, **26**(3)

Tennant C (2012) *Nine decades of glacier change in the Canadian Rocky Mountains*. April, ISBN 9780494875445

Tennant C and Menounos B (2013) Glacier change of the Columbia Icefield, Canadian Rocky Mountains, 1919-2009. *J. Glaciol.*, **59**(216), 671–686, ISSN 00221430 (doi: 10.3189/2013JoG12J135)

Van Wychen W, Copland L, Jiskoot H, Gray L, Sharp M and Burgess D (2018) Surface Velocities of Glaciers in Western Canada from Speckle-Tracking of ALOS PALSAR and RADARSAT-2 data. *Can. J. Remote Sens.*, **44**(1), 57–66, ISSN 17127971 (doi: 10.1080/07038992.2018.1433529)